

1 Holographic Metalens for Switchable Focusing of Surface Plasmons

2 Daniel Wintz,[†] Patrice Genevet,^{†,‡} Antonio Ambrosio,^{†,§} Alex Woolf,[†] and Federico Capasso^{*,†}

3 [†]School of Engineering and Applied Sciences, Harvard University, 9 Oxford Street, McKay 125, Cambridge, Massachusetts 02138
4 United States

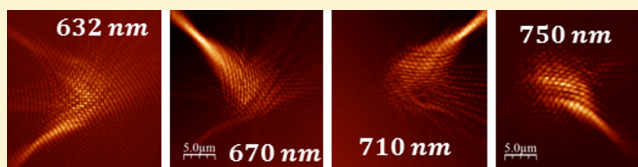
5 [‡]Singapore Institute of Manufacturing Technology, 71 Nanyang Drive, Singapore 638075, Singapore

6 [§]CNR-SPIN U.O.S. Napoli, Dipartimento di Fisica, Università di Napoli Federico II, Complesso Universitario di Monte Sant'Angelo,
7 Via Cintia, 80126 - Napoli, Italy

8 **S** Supporting Information

9 **ABSTRACT:** Surface plasmons polaritons (SPPs) are light-
10 like waves confined to the interface between a metal and a
11 dielectric. Excitation and control of these modes requires
12 components such as couplers and lenses. We present the
13 design of a new lens based on holographic principles. The key
14 feature is the ability to switchably control SPP focusing by
15 changing either the incident wavelength or polarization. Using
16 phase-sensitive near-field imaging of the surface plasmon wavefronts, we have observed their switchable focusing and steering as
17 the wavelength or polarization is changed.

18 **KEYWORDS:** *Metasurfaces, surface plasmons, holography, metalens*



19 **S**urface plasmon polaritons (SPPs) are electromagnetic
20 surface waves confined to propagate at the interface of a
21 metal and a dielectric, involving both a charge oscillation of free
22 electrons in the metal and an evanescent electric field extending
23 into the dielectric.¹ SPPs have garnered attention for decades
24 now, affording the possibility to control light at the nanoscale,
25 transfer information on subwavelength scales, and other novel
26 optical techniques.^{2–4} Coupling into SPP modes can be
27 accomplished by simple experimental configurations, typically
28 by using prism geometries or diffractive gratings. In addition,
29 the development of high-resolution lithography and milling
30 techniques allows for the design of structures that can be
31 integrated into complex optoelectronic circuits whose function-
32 ality is based on the processing of SPPs. Recently developed
33 nanostructured surfaces (metasurfaces) that control the
34 amplitude, phase, and polarization of propagating light or
35 SPPs are particularly suited for wavefront engineering.^{5–9}
36 Metasurfaces based on plasmonics have already been used to
37 implement flat lenses that work in transmission^{10–13} or in
38 reflection^{14,15} with reduced aberrations.^{16,17} On the metal–
39 dielectric interface, wavelength selective focusing^{18,19} and
40 unidirectional coupling to plane waves²⁰ have also been
41 shown by means of plasmonic couplers made of nanoslits.
42 Nanoholes and nanoslits are among the most commonly used
43 unit elements when designing metasurfaces for SPP manipu-
44 lation.^{21–24}

45 Here, we demonstrate a metalens design strategy based on
46 holographic principles. The metalens has the ability to steer
47 SPPs between several foci on the surface based on the incident
48 wavelength and has on/off switchability based on the incident
49 polarization. Our design is straightforward and consists of
50 placing nonresonant nanoslits (50 nm wide, 200 nm long)

along the contours defined by the wavefront of SPPs
51 propagating out from an imaginary emitter placed at the
52 location on the surface where we want SPP focusing. The
53 imaginary point source is treated as a Huygens' emitter that can
54 be described by a simple 2D circular wave: $\vec{E} \propto e^{ik_{\text{SPP}}r}$, where k_{SPP}
55 is the wavevector of the SPP at gold/air interface and r is the
56 distance from the imaginary source point (Figure 1). Because
57 if the nanoslits lie on the equiphase lines (wavefront of the SPPs),
58 if the nanoslits are excited in phase then the reradiated SPPs
59 will constructively interfere at the position of the original
60 imaginary emitter. Because we want to have multiple foci (for
61 tunability purposes), adding another focus requires the
62 nanoslits to be placed not just on the equiphase lines of one
63 imaginary emitter but on the equiphase points resulting from
64 the intersections of the wavefronts of all the imaginary point
65 sources (Figure 1). In our device, a different source point for
66 each free space wavelength (632, 670, 710, and 750 nm) is
67 chosen such that light at each wavelength couples to SPPs via
68 the nanoslits and is focused to the four corners of a $16 \mu\text{m} \times 16$
69 μm square. In Figure 1a,b, the mutual wavefront intersections
70 are denoted by the black dots, which are the positions where we
71 mill nanoslits in the gold film.

72 Interestingly, our approach is a special case of a more general
73 design principle based on holography,^{25–27} which has been
74 extended for use with surface plasmons.^{28–37} In general,
75 holography involves recording the interference pattern between
76 a suitably chosen reference wave and the light scattered by an
77 object into a photosensitive material. Both intensity and phase
78

Received: March 18, 2015

Revised: April 23, 2015

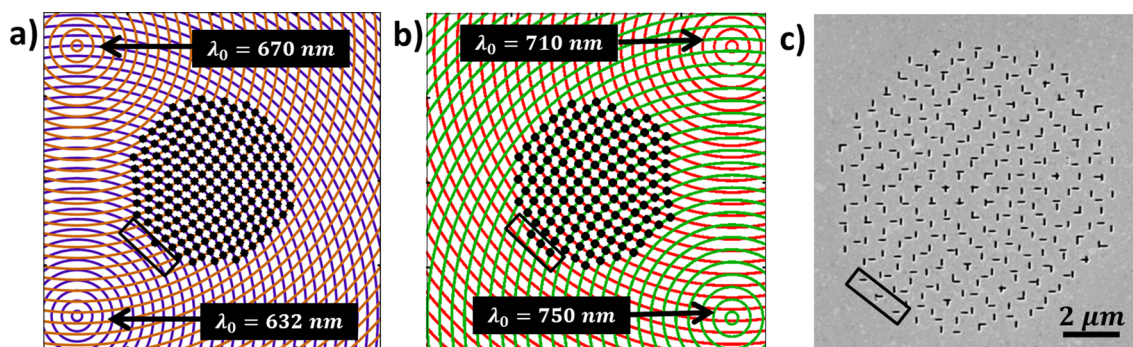


Figure 1. Metalens design. (a) Focal points for illuminating light wavelengths $\lambda_0 = 632$ and 670 nm in the bottom and top left corners, respectively. Purple circles denote the wavefronts of an imaginary circular point source located in the bottom left corner for $\lambda_0 = 632$ nm ($\lambda_{\text{SPP}} = 604$ nm). Orange circles denote the wavefront for $\lambda_0 = 670$ nm imaginary source in the top left corner. Black dots denote the intersections of the two wavefronts (within a $5 \mu\text{m}$ radius), which is where vertical nanoslits are milled. Vertical nanoslits couple light into surface plasmon polaritons preferentially when excited with normally incident horizontally polarized light. Thus, if the vertical apertures are illuminated with the latter at $\lambda_0 = 632$ or 670 nm light, all of the scattered surface plasmons that reach the respective focal point (on the left side) will be in phase because by design they lie on the equiphase lines. (b) Equivalent of panel a but for the other two wavelengths ($\lambda_0 = 710$ and 750 nm), which will be focused to the remaining corners of the $16 \mu\text{m} \times 16 \mu\text{m}$ square. Black circles in panel b denote where horizontal nanoslits are milled. There are fewer intersection (equiphase) points because the wavelengths are longer. (c) Scanning electron micrograph of our device after the nanoslits are etched into the gold film by focused ion beam. Even though some of the nanoslits overlap, this does not appreciably affect the performance of the device. The black box is shown for reference and denotes the same physical space in all panels.

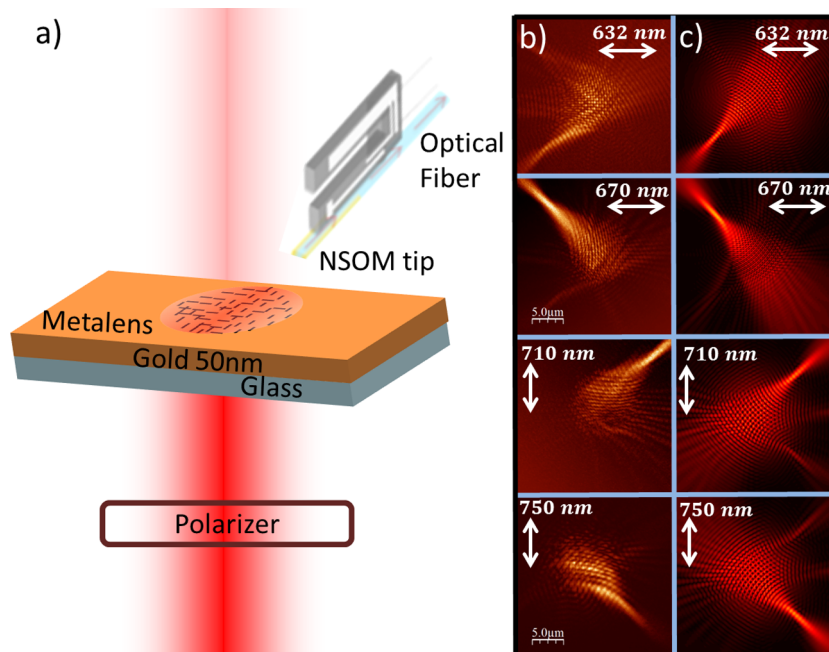


Figure 2. Experimental setup and results. (a) Experimental setup; light from a supercontinuum laser source is incident on the sample from below. Light at a single wavelength is passed through a polarizer in order to set the incident light polarization, and the light is focused onto the metalens (not depicted). Some of the laser light is transmitted, which can produce an interference pattern in the data depending on the relative intensities of the SPPs and the transmitted light. NSOM is used to collect light. The NSOM tip, which is a metal-coated, tapered optical fiber, interacts with the evanescent field of the SPP and scatters it, converting energy from the SPP mode into a propagating waveguide mode in the optical fiber. (b) Experimental results with the polarization of light denoted by the white arrow. SPP beams are unidirectionally focused to the four corners of a square depending on the wavelength and polarization. (c) Analytical simulations used to compare to the experimental results. Each aperture (with the correct orientation) in the metalens is treated as a point dipole and the fields from all the nanoslits are summed to give the in-plane total electric field.

79 information on the object's scattered wavefront can be retrieved
80 by illuminating the recorded interference pattern with the
81 reference beam. In regards to our device, the equiphase lines
82 (on which the nanoslits are placed) are equivalent to the lines
83 of constructive interference between a flat wavefront (e.g., a
84 normally incident plane wave) and a circular point source,
85 where the flat wavefront assumes the holographic role of the

suitably chosen reference wave and the SPP from the imaginary 86
point source assumes the role of the light scattered by an 87
object. It is worth noting here that an iterative algorithm is not 88
needed;^{18,38} most holographic approaches utilize such algo- 89
rithms to maximize the constructive interference between 90
antennas. Moreover, as these algorithms only aim to maximize 91
the intensity at a specific position, they do not necessarily result 92

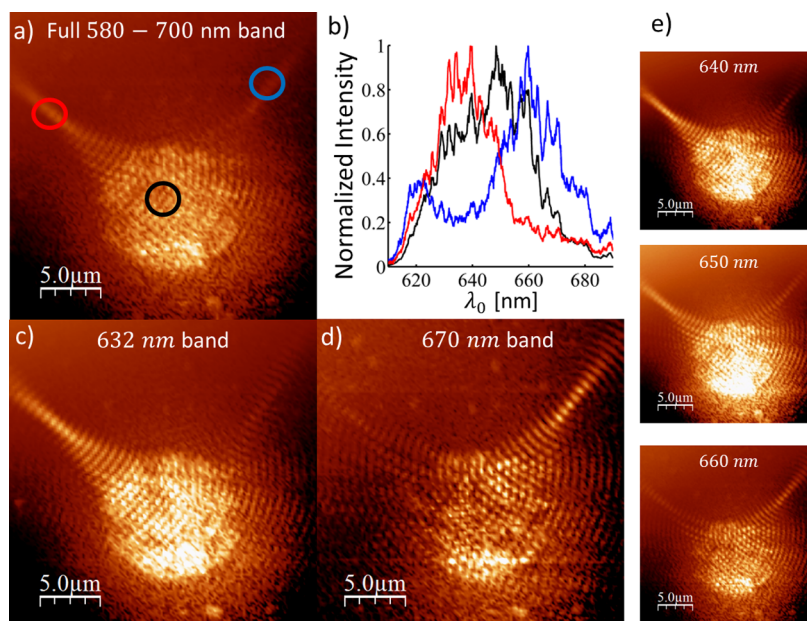


Figure 3. Spectrally resolved NSOM imaging. A single NSOM scan is performed while the metalens is illuminated with $\lambda_0 = 580\text{--}700$ nm. The same experimental setup as in Figure 2a is used except the optical fiber connected to a spectrometer. (a) Spectrally resolved NSOM image for the whole wavelength range; each pixel in the image represents the number of counts in a wavelength range of 580–700 nm (the full band). The colored circles in (a) correspond to the physical location on the metalens where the colored spectra (b) are taken, that is, the black spectrum from (b) is taken inside the black circle in (a). Each curve in (b) is normalized independently to highlight the spectral shifts. (c) Spectrally resolved NSOM image for a band of 632 ± 3 nm. Each pixel intensity represents the sum of all photon counts within that wavelength range. (d) Same as in panel c but for a wavelength range 670 ± 3 nm. (e) Spectrally resolved data for wavelength bands in between the operating wavelengths. A unique characteristic of the device is that the power is always concentrated into the two directions but with different relative intensities that depend on how close the wavelength is to the two operating wavelengths (632 and 670 nm).

93 in a propagating beam of light, producing intense hot-spots
94 instead. Furthermore, our approach allows us to choose the
95 phase of the SPPs at the focus (relative to the incident beam),
96 since the initial choice of point source phase is arbitrary. This
97 can be important if a specific phase is needed, for instance, to
98 couple the SPPs to a specific plasmonic waveguide mode or
99 other components of a more complex circuit located at the
100 focal positions.

101 Another central point of our design is to use nanoslits instead
102 of nanoholes for coupling light to SPPs. Light passing through a
103 nanoaperture diffracts, giving rise to a large spread of
104 wavevectors that allows coupling into SPP modes. A nanoslit
105 that is subwavelength predominantly in one direction radiates
106 SPPs preferentially when the incident light is polarized normal
107 to the slit. Far from the nanoslit (several hundred nanometers),
108 the SPP intensity has a simple dipole-like distribution.
109 Nanoholes can couple free space light to SPPs, but they do
110 so without polarization selectivity. Employing nanoslits adds
111 polarization selectivity because light polarized perpendicular to
112 the nanoslit couples preferentially. Horizontal nanoslits are
113 excited by vertically polarized light and vice versa, which forms
114 the basis for the polarization on/off selectivity and polarization
115 tunable coupling of the metalens. Each orientation (horizontal
116 or vertical) of nanoslits in the device has two operating free
117 space wavelengths; vertical slits couple to $\lambda_0 = 632$ and $\lambda_0 = 670$
118 nm, horizontal slits couple to $\lambda_0 = 710$ and $\lambda_0 = 750$ nm.
119 Wavelength tunable directionality is based on the following: for
120 a set of slits, if one of the operating wavelengths with the
121 correct polarization is incident on the device, the only location
122 where all of the SPPs constructively interfere is the original
123 imaginary source point; nowhere else will all of the SPPs

constructively interfere. These slits are shown in the scanning
124 electron micrograph (SEM) of Figure 1c. 125

To fabricate our device, we e-beam evaporate a 50 nm film of
126 gold onto a polished silicon wafer and template strip³⁹ it onto a
127 glass slide for decreased surface roughness. Then, after
128 following the design depicted in Figure 1, we use focused ion
129 beam (FIB) milling to etch the nanoslits into the gold film
130 (Figure 1c). The sample is illuminated from below with linearly
131 polarized light (Figure 2). The illuminating beam is at normal
132 incidence and focused (beam waist of ~ 10 μm) on the
133 metalens. The incident light is emitted from a super continuum
134 laser with a wavelength range in the band 400–850 nm. This
135 laser excites the nanoslits causing SPP emission while the probe
136 of a near-field scanning optical microscope (NSOM) scans an
137 area of the surface that includes the metalens and the focal
138 points. Our NSOM (Nanonics Imaging Multiview) probe is a
139 metal-coated, tapered optical fiber with a subwavelength
140 aperture at the facet. The NSOM probe interacts with the
141 evanescent field of the SPPs close to the metal/air interface that
142 are then coupled into propagating modes in the optical fiber
143 (collection mode NSOM). The other end of the fiber is
144 connected to a single photon avalanche photodiode (SPAD) or
145 a spectrometer. Figure 2a presents a full schematic of the
146 experimental setup. 147

Since the metallic film in our device is optically thin (40–50
148 nm), some of the incident light is transmitted through the
149 sample. This transmitted light interferes with the SPPs at the
150 surface such that the signal recorded by the NSOM at each
151 pixel is the SPP intensity modulated by this interference. This
152 useful effect allows for direct imaging of the wavefronts of the
153 focusing SPP beam without any external reference beam or
154 interferometric setups. Figure 2b shows the operation of the 155

156 device when illuminated by light with the correct polarization
157 and wavelength from the laser source (one polarization and
158 wavelength at a time). Directional focusing of SPPs on the
159 surface is evident as the different wavelengths are focused to the
160 four corners of a square.

161 In order to better understand our experimental results, we
162 implemented an analytical model of how the designed metalens
163 will function. We treat each nanoslit as an infinitesimal perfect
164 electric point dipole with a direction of emission perpendicular
165 to the slit, such that a vertical nanoslit is represented by a
166 horizontal dipole. Adapting eq 2 from ref 18, we then sum the
167 contribution from each antenna

$$E_{\text{total}} = \sum_i \frac{e^{jk_{\text{SPP}}[(x-x_i)^2+(y-y_i)^2]^{1/2}}}{[(x-x_i)^2+(y-y_i)^2]^{3/4}} [(x-x_i)\cos(\eta) - (y-y_i)\sin(\eta)] \quad (1)$$

168 where k_{SPP} is the wavenumber of the surface plasmon, x_i, y_i is the
170 position of the i th dipole, and η is the angle of orientation of
171 the nanoslit relative to the vertical: 0 for vertical apertures and
172 $\pi/2$ for horizontal apertures. This total field is then added to
173 the electric field produced by a flat wavefront, representing our
174 focused Gaussian beam at the focal plane. Implementation and
175 comparison of this analytical model to the experimental results
176 can be seen in Figure 2b,c. The agreement between the data
177 and the analytical model suggests that multiple reflections of
178 SPPs from the nanoslits are not a serious factor in the
179 performance of the device, as the model does not take this into
180 account. Furthermore, an effective numerical aperture (NA)
181 can be defined according to $\text{NA} = (\lambda_{\text{SPP}}/\pi w)$ where $2w$ is the
182 full width at half-maximum of the beam at the focus. The
183 effective NA for the metalens with this definition is calculated
184 to be on average 0.68 for the operating wavelengths. The full
185 width at half-maximum at the focus for all the wavelengths is
186 roughly λ_{SPP} . Reminiscent of the diffraction limit, this waste
187 could be decreased by fabricating a larger metalens; a larger
188 diameter metalens would include more wavevectors and
189 recreate the point source more accurately. We note that the
190 nanoslits closest to the focal point will contribute more than the
191 nanoslits that are further, mainly due to their dipolar nature (eq
192 1) and their propagation losses (see Supporting Information).

193 In order to calculate the relative efficiency of the metalens, it
194 is useful to compare it to an isotropic scatterer of SPPs (for
195 example, radially or circularly polarized light incident onto a
196 circular aperture). The percentage of SPPs contained within a
197 given angle θ of the isotropic scatterer is simply given by $\theta/$
198 360° . To compare this to our device, we measure the intensity
199 of SPPs as a function of θ along the circumference of a circle
200 with radius equal to the focal distance, $11.3 \mu\text{m}$. We find that
201 on average 23% of the SPPs at the focal radius are contained
202 within a 10° angle, which is almost an order of magnitude
203 higher than the isotropic scatterer, which only contains 2.8% of
204 the SPP intensity within a 10° angle.

205 In order to further characterize our metalens, we illuminated
206 the sample with a wide band (580–700 nm), chosen to include
207 two of the operating wavelengths. In this case, the NSOM fiber
208 is connected to a spectrometer (Andor Shamrock and Newton
209 EMCCD Camera). The spectrally resolved NSOM data are
210 presented in Figure 3. Interestingly, the SPPs are always
211 concentrated into the two different channels but with different
212 relative intensities. For example, while $\lambda_0 = 632$ and 670 nm
213 light are almost completely concentrated into a single direction

(following the original design), 650 nm light is split between
214 two directions (Figure 3e). This behavior, imposed by the
215 design, can be understood by noting that the difference in SPP
216 wavelengths is small compared to λ_{SPP} , (~ 20 nm for $\lambda_0 = 632$
217 and 650 nm light). When excited by 650 nm light, the apertures
218 are only slightly offset from the equiphase lines in Figure 1a,
219 and their emissions will constructively interfere at the source
220 points (though not as completely as it does for 632 and 670
221 nm). In addition, this explains why the power transfers from
222 one direction to the other as λ_{SPP} gets closer to or further away
223 from one of the operating wavelengths. For example, 640 nm
224 light concentrates more power in the 632 nm channel and less
225 into the 670 nm channel; however, 660 nm light experiences
226 the opposite. In terms of applications, monitoring the relative
227 intensities in each arm would allow for an on-chip
228 spectrometer.

229 Figure 4 shows the focusing of the SPPs and characterizes the
230 polarization on/off switching. In Figure 4a, the interference of
231

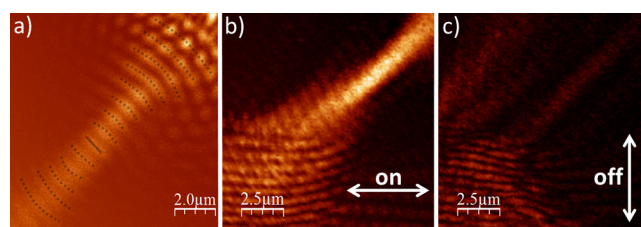


Figure 4. Focusing and polarization on/off switching. (a) NSOM image of the focal point when the metalens is illuminated with 750 nm light with vertical polarization. Superimposed are black dashed lines that highlight the wavefront curvature as the beam focuses, with the focus denoted by the solid black line. Note the single apertures in the top right portion of the image that act as surface plasmon polariton (SPP) sources (together with all the others in the device). (b) SPP beam focusing for $\lambda_0 = 710$ nm when the metalens is illuminated with the “on” polarization (horizontal). (c) Same as panel b but with the metalens illuminated with the “off” polarization (vertical). The ratio of the intensities at the foci of (b) and (c) are 15:1, giving 12 dB of modulation.

the incident beam and focusing SPPs is shown in order to view
232 the SPP wavefronts during focusing. In Figure 4b, the metalens
233 is illuminated with the polarization that maximizes coupling
234 into SPP modes. For comparison, Figure 4c shows the metalens
235 when illuminated with a polarization that is parallel to the
236 associated nanoslits, minimizing the coupling to SPPs.

237 In this paper, we demonstrated a metalens design strategy
238 that can be used to overcome some of the coupling and
239 focusing issues for SPPs. The design strategy can be used to
240 gain both wavelength and polarization tunability over the
241 direction of SPP beam propagation; most importantly, by
242 recreating the wavefront of a point source we are able to focus
243 SPP beams after coupling. The metalens is studied under both
244 single wavelength illumination (collecting intensity) and
245 broadband illumination (collecting spectrally resolved inten-
246 sity) with phase information in certain cases. Free space light is
247 coupled to a nanostructured surface via subwavelength slits and
248 steered into different directions based on its wavelength and
249 polarization in the form of a focused SPP beam. We note that
250 the relative efficiency of our metalens as compared to an
251 isotropic coupler is improved by an order of magnitude. Also,
252 the coupling conversion efficiency can be improved by
253 optimizing the nanoslit geometry to take advantage of a
254 plasmonic resonance. We show phase evolution of the created
255

256 SPP beams and highlight the focusing. In principle, these beams
 257 could be easily outcoupled and reradiated back into free space
 258 modes, which would serve to completely demultiplex free space
 259 light of different wavelengths, accomplished by a single,
 260 ultrathin optical element. The design strategy presented here
 261 could open up new opportunities in the realms of integrated
 262 waveguides, on-chip spectroscopy, or broadband demulti-
 263 plexers.

264 ■ ASSOCIATED CONTENT

265 ● Supporting Information

266 Design figures of merit, angular intensity distribution
 267 calculation, analytical calculations under varying angles of
 268 incidence, and data on a two polarization and two wavelength
 269 device are available. The Supporting Information is available
 270 free of charge on the ACS Publications website at DOI:
 271 10.1021/acs.nanolett.5b01076.

272 ■ AUTHOR INFORMATION

273 Corresponding Author

274 *E-mail: capasso@seas.harvard.edu.

275 Funding

276 The authors acknowledge support from the Harvard Nanoscale
 277 Science and Engineering Center (NSEC) under contract NSF/
 278 PHY 06-46094, and the Center for Nanoscale Systems (CNS)
 279 at Harvard University, which is a member of the National
 280 Nanotechnology Infrastructure Network (NNIN). This work
 281 was supported by a National Science Foundation Early concept
 282 Grant for Exploratory Research (Grant ECCS-1347251), and
 283 by the Air Force Office of Scientific Research under Grant
 284 FA9550-12-1-0289.

285 Notes

286 The authors declare no competing financial interest.

287 ■ ACKNOWLEDGMENTS

288 The authors would like to acknowledge useful discussions with
 289 R. Zhang, M. Katz, and J-P. B. Mueller. The authors
 290 acknowledge E. Orabona for the MATLAB routine used on
 291 the spectrally resolved NSOM data. The authors acknowledge
 292 Nanonics Ltd. and Andor Technology for support in the near-
 293 field setup and spectral imaging, respectively.

294 ■ REFERENCES

- 295 (1) Maier, S. A. *Plasmonics: Fundamentals and Applications*; Springer
 296 Science and Business Media: New York, 2007.
 297 (2) Shalaev, V. M.; Kawata, S. *Nanophotonics with Surface Plasmons*;
 298 Elsevier: Oxford, 2006.
 299 (3) Barnes, W. L.; Dereux, A.; Ebbesen, T. W. *Nature* **2003**, *424*,
 300 824–830.
 301 (4) Ozbay, E. *Science* **2006**, *113*, 189–193.
 302 (5) Yu, N.; Genevet, P.; Kats, M. A.; Aieta, F.; Tetienne, J. P.;
 303 Capasso, F.; Gaburro, Z. *Science* **2011**, *334*, 333–337.
 304 (6) Ni, X.; Emani, N. K.; Kildishev, A. V.; Boltasseva, A.; Shalaev, V.
 305 M. *Science* **2012**, *335*, 427–427.
 306 (7) Yu, N.; Capasso, F. *Nat. Mater.* **2014**, *13*, 139–150.
 307 (8) Yu, N.; Aieta, F.; Genevet, P.; Kats, M. A.; Gaburro, Z.; Capasso,
 308 F. *Nano Lett.* **2012**, *12*, 6328–6333.
 309 (9) Pors, A.; Nielsen, M. G.; Bozhevolnyi, S. I. *Opt. Lett.* **2013**, *38*,
 310 513–515.
 311 (10) Ni, X.; Ishii, S.; Kildishev, A. V.; Shalaev, V. M. *Light: Sci. Appl.*
 312 **2013**, *2*, 1–5.
 313 (11) Chen, X.; Huang, L.; Muhlenbernd, H.; Li, G.; Bai, B.; Qiaofeng,
 314 T.; Guofan, J.; Cheng-Wei, Q.; Zhang, S.; Zentgraf, T. *Nat. Commun.*
 315 **2012**, *3*, 1198–1203.

- (12) Kang, M.; Feng, T.; Wang, H. T.; Li, J. *Opt. Express* **2012**, *20*,
 15882–15890. 317
 (13) Babak, M.; Mosallaei, H. *Opt. Lett.* **2011**, *36*, 2569–2571. 318
 (14) Li, X.; Xiao, S.; Cai, B.; He, Q.; Cui, T. J.; Zhou, L. *Opt. Lett.*
2012, *37*, 4940–4942. 319
 (15) Pors, A.; Nielsen, M. G.; Eriksen, R. L.; Bozhevolnyi, S. I. *Nano*
Lett. **2013**, *13*, 829–834. 321
 (16) Aieta, F.; Genevet, P.; Kats, M. A.; Yu, N.; Blanchard, R.;
 Gaburro, Z.; Capasso, F. *Nano Lett.* **2012**, *12*, 4932–4936. 322
 (17) Aieta, F.; Genevet, P.; Kats, M. A.; Capasso, F. *Opt. Express*
2013, *21*, 31530–31539. 323
 (18) Tanemura, T.; Balram, K. C.; Ly-Gagnon, D. S.; Wahl, P.;
 White, J. S.; Brongersma, M. L.; Miller, D. A. *Nano Lett.* **2011**, *11*,
 2693–2698. 324
 (19) Chen, Y. G.; Yang, F. Y.; Liu, J.; Li, Z. Y. *Opt. Express* **2014**, *22*,
 14727–14737. 325
 (20) Lin, J.; Mueller, J. B.; Wang, Q.; Yuan, G.; Antoniou, N.; Yuan,
 X. C.; Capasso, F. *Science* **2013**, *340*, 331–334. 326
 (21) Lee, K. G.; Park, Q. H. *Phys. Rev. Lett.* **2005**, *95*, 1039021–
 1039024. 327
 (22) López-Tejiera, F.; Rodrigo, S. G.; Martin-Moreno, L.; Garcia-
 Vidal, F. J.; Devaux, E.; Ebbesen, T. W.; Krenn, J. R.; Radko, I. P.;
 Bozhevolnyi, S. I.; Gonzalez, M. U.; Weeber, J. C.; Dereux, A. *Nat.*
Phys. **2007**, *3*, 324–328. 328
 (23) Liu, Z.; Steele, J. M.; Srituravanich, W.; Pikus, Y.; Sun, C.;
 Zhang, X. *Nano Lett.* **2005**, *5*, 1726–1729. 329
 (24) Yin, L.; Vlasko-Vlasov, V. K.; Pearson, J.; Hiller, J. M.; Hua, J.;
 Welp, U.; Brown, D. E.; Kimball, C. W. *Nano Lett.* **2005**, *5*, 1399–
 1402. 330
 (25) Gabor, D. *Proc. R. Soc. London, Ser. A* **1949**, 454–487. 331
 (26) Denisjuk, Y. N. *Sov. Phys.-Dokl.* **1962**, *7*, 543–548. 332
 (27) Leith, E. N.; Upatnieks, J. *J. Opt. Soc. Am.* **1962**, *52*, 1123–1128. 333
 (28) Cowan, J. J. *Opt. Commun.* **1972**, *5*, 69–72. 334
 (29) Maruo, S.; Nakamura, O.; Kawata, S. *Appl. Opt.* **1997**, *36*,
 2343–2346. 335
 (30) Wang, G. P.; Sugiura, T.; Kawata, S. *Appl. Opt.* **2001**, *40*, 3649–
 3653. 336
 (31) Genevet, P.; Capasso, F. *Rep. Prog. Phys.* **2015**, *78*, 024401–
 024420. 337
 (32) Ozaki, M.; Kato, J.; Kawata, S. *Science* **2011**, *332*, 218–220. 338
 (33) Genevet, P.; Lin, J.; Kats, M. A.; Capasso, F. *Nat. Commun.*
2012, *3*, 1278. 339
 (34) Dolev, I.; Epstein, I.; Arie, A. *Phys. Rev. Lett.* **2012**, *109*,
 2039031–2039035. 340
 (35) Ni, X.; Kildishev, A. V.; Shalaev, V. M. *Nat. Commun.* **2013**, *4*,
 2807. 341
 (36) Zhou, F.; Liu, Y.; Cai, W. *Opt. Express* **2013**, *21*, 4348–4354. 342
 (37) Huang, L.; Chen, X.; Muhlenbernd, H.; Zhang, H.; Chen, S.;
 Bai, B.; Tan, Q.; Jin, G.; Cheah, K. W.; Qiu, C. W.; Li, J.; Zentgraf, T.;
 Zhang, S. *Nat. Commun.* **2013**, *4*, 2808. 343
 (38) Orabona, E.; Ambrosio, A.; Longo, A.; Carotenuto, G.; Nicolais,
 L.; Maddalena, P. *Opt. Lett.* **2014**, *39*, 4263–4266. 344
 (39) Hegner, M.; Wagner, P.; Semenza, G. *Surf. Sci.* **1993**, *291*, 39–
 46. 345